Cold sintering yields first layered double hydroxides (LDH) monolithic materials

Hyoung-Jun Kim, Tae-Hyun Kim, Jae-Min Oh, Fabrice Salles, Geoffroy Chevallier, Carole Thouron, Philippe Trens, Jérémy Soulie, Sophie Cazalbou, Christophe Drouet

Revised manuscript (revision #1, Jan 2022)

Cold Sintering Yields First Layered Double Hydroxides (LDH) Monolithic Materials

Hyoung-Jun KIM,[a] Tae-Hyun KIM,[b] Jae-Min OH,*[,c] Fabrice SALLES,[d] Geoffroy CHEVALLIER,[e] Carole THOURON,[f] Philippe TRENS,[d] Jérémy SOULIE,[f] Sophie CAZALBOU,[f] and Christophe DROUET,*[,f]

[a]Research Institute, National Cancer Center, 323 Ilsan-ro, Goyang, Gyeonggi 10408, Republic of Korea.

[b]Department of Environmental Engineering, Seoul National University of Science and Technology, Seoul 01811, Republic of Korea.

[c]Department of Energy and Materials Engineering, Dongguk University, Seoul, Republic of Korea, E-mail: jaemin.oh@dongguk.edu.

[d]ICGM, Univ. Montpellier, CNRS, ENSCM, Montpellier, France.

[e]PNF² / CIRIMAT, Université Toulouse 3 Paul Sabatier, 118 route de Narbonne, FR-31029, Toulouse, France.

[f]CIRIMAT, Université de Toulouse (CNRS / INP / UT3), Ensiacet, 4 allée Emile Monso,FR-31030, Toulouse, France. E-mail: christophe.drouet@cirimat.fr

Abstract

Layered double hydroxides (LDHs) are key inorganic compounds relevant to a wealth of applicative purposes, by exploiting their layered structure allowing for ion/molecular sequestration or release. However, a technological barrier exists in the fabrication of

cohesive LDH monoliths in link with their metastability. In this work, a series of cohesive monoliths of different LDH ionic compositions and structures (namely hydrotalcite, pyroaurite and hydrocalumite) were successfully obtained for the first time, using cold sintering via spark plasma sintering (SPS) at 130 °C. Thanks to the low temperature involved in this non-conventional consolidation approach, the structure and chemical stability of the LDHs are preserved and allow preparing densified LDH scaffolds with internal cohesion, as evidenced by densification rates often above 80 %, SEM microstructural observations and mechanical testing assessments, mainly due to a better alignment of adjacent layered particles. By way of water vapor sorption measurements, we demonstrate that the interfacial/interlayer spaces of the LDH structure remain accessible after cold sintering. Also, the porous network of the monoliths and related access to interfacial surface are shown to be tunable by adding a leachable pore-forming agent such as SiO_2 beads. Possible sintering mechanisms are discussed by complementary experiments-simulations coupling, unveiling the role of LDH composition as in the case of Cl-bearing LDH. By overcoming the challenge of monolith fabrication out of LDH compounds, applications are expected to benefit from these findings, as in electronics, energy storage, catalysis, biomaterials and depollution.

Keywords: LDH, monoliths, cold sintering, SPS, simulation, sorption

1. Introduction

Layered double hydroxides (LDHs) are a major family of mineral compounds, which have lately attracted great attention [1]. Their lamellar structure is composed of parallel M^{2+}/M^{3+} metal hydroxide sheets with intercalated A^{m-} anions and water molecules, corresponding to the general formula $[(M^{2+})_{1-x}(M^{3+})_x(OH)_2]^{x+}[(A^{m-})_{x/m}(H_2O)_n]^{x-}$ (**Figure S1**). Among relevant

characteristics are their tunable ionic composition, their flexibility in terms of molecular intercalation and the consequential modularity of their physical, chemical and biological properties. Whether natural or synthetic, their relevance in a wealth of applications has been evidenced, in environmental sciences as in depollution systems, sorbents, catalysis, but also in other domains like nanomedicine, supercapacitors, flame retardants, light emitters, electrochemical sensing, etc. [2-10].

To date, such applications have been mainly explored using LDHs in the form of dispersed nanoparticles [11-14], microparticles [15], nanosheets [4], thin films [16], or in aerogel composites [17]. Very few consolidated monolithic LDH have been reported and only at high temperatures [6, 18]. Systems based on LDH particles or gel drying led to non-cohesive assemblies [15]. LDH-based highly porous xerogels were reported for the remediation of toxic oxyanions [19, 20], but they were not associated with any consolidation process, thus remaining non-cohesive.

Although LDH systems have demonstrated their significance for the applicative purposes listed above, the possibility to consolidate LDHs into genuine 3D pieces thus remains a technological challenge due to its metastability toward thermal treatment; yet, being able to obtain, manipulate, cut and assemble large pieces of LDH materials could i) facilitate the development and industrialization of existing usages and ii) open avenues of further applications of LDHs in the form of 3D monoliths for supported catalysis, solid electrolytic membrane, orthopedic implants, depollution filters, chromatography separation, nuclear waste storage, etc.

In this context, non-conventional consolidation processes at low temperature are needed, similarly to the case of nanocrystalline and hydrated biomimetic calcium phosphate apatites, for which heating beyond 150 °C causes significant nanocrystals alterations [21]. Cold sintering by spark plasma sintering (SPS) at 150 °C was found, since 2006, to allow successful consolidation of apatite nanocrystals by exploiting the mobility of internal water molecules and

surface ions, while preserving the nanosized and hydrated characteristics of the starting powder [21-23]. Cold sintering exploiting the presence of a fluid component has been declined to other materials [24] and generated recently immense interest in many fields as in ferroelectrics, 5G development, etc. [24-26].

The eventuality of obtaining actual LDH consolidated monoliths via cold SPS sintering was investigated in the present work. Related features of the sintered bodies were then explored in terms of structure, morphology, mechanical resistance, N_2 and water adsorption. A computational approach was also developed for relating the experimental sinterability of LDHs to the mechanical properties of layers (bulk modulus) as a function of the chemical composition. Finally, possible mechanisms for LDH cold sintering are discussed.

2. Materials and Methods

2.1. Raw materials

Magnesium nitrate hexahydrate ($Mg(NO_3)_2 \cdot 6H_2O$), aluminum nitrate nonahydrate ($Al(NO_3)_3 \cdot 9H_2O$), iron (III) nitrate nonahydrate ($Fe(NO_3)_3 \cdot 9H_2O$) and iron (III) chloride hexahydrate ($FeCl_3 \cdot 6H_2O$) sodium bicarbonate ($NaHCO_3$) and urea ($CO(NH_2)_2$) were obtained from Sigma-Aldrich Inc (St. Louis, MO, USA). Calcium chloride dihydrate ($CaCl_2 \cdot 2H_2O$) was obtained from Junsei Chemical Co., Ltd. Sodium hydroxide (NaOH) was purchased from Daejung Chemicals & Metals Co. LTD. (Siheung, Gyeonggi, Korea).

2.2. LDH synthesis

Hydrotalcite (MgAl-CO_3 LDH) powders with varying particle sizes – Hydrotalcite LDH powders with small (LDH-S) and medium (LDH-M) particle sizes were prepared by coprecipitation and subsequent hydrothermal reaction. The mixed metal solution of 0.45 M $Mg(NO_3)_2 \cdot 6H_2O$ and 0.225 $Al(NO_3)_3 \cdot 9H_2O$ was titrated with a base solution (0.675 M NaOH/0.506 M $NaHCO_3$) until pH reached at 9.5. The obtained precipitate was transferred to a hydrothermal bomb and then treated at 100°C for 12h and at 150°C for 24h, respectively for small (LDH-S) and medium (LDH-M) sized LDH.

LDH powder with large particle size (LDH-L) was prepared through urea hydrolysis method. The metal solution (0.2 M $Mg(NO_3)_2 \cdot 6H_2O$ /0.1 M $Al(NO_3)_3 \cdot 9H_2O$) was mixed with 1.39 M urea solution and then aged at 90°C for 24h. The prepared slurry was transferred to stainless steel bomb and treated at 100°C for 12h (LDH-L). The final product was washed with deionized water and lyophilized.

Pyroaurite (MgFe-CO_3-LDH) powder – MgFe-CO_3-LDH (pyroaurite crystal structure, $Mg_6Fe_2(OH)_{16}CO_3 \cdot 4.5H_2O$) was synthesized as follows: the mixed metal solution of 0.25 M $Mg(NO_3)_2 \cdot 6H_2O$ and 0.125 M $Fe(NO_3)_3 \cdot 9H_2O$ was titrated with alkaline solution (1 M NaOH/0.3 M $NaHCO_3$) until pH reached 9.5. Then, the obtained precipitate was washed with deionized water and lyophilized.

Hydrocalumite-like (CaFe-Cl-LDH) powder – CaFe-Cl-LDH (hydrocalumite-like crystal structure, $Ca_2Fe(OH)_6Cl \cdot 2H_2O$) was synthesized as follows: the mixed metal solution of 0.315 M $CaCl_2 \cdot 2H_2O$ and 0.157 M $FeCl_3 \cdot 6H_2O$ was titrated with 1.26 M NaOH solution until pH reached 12.5. Then, the obtained precipitate was washed with deionized water and lyophilized.

Addition of pore-forming agent – For exploring the possibility to further modulate the porosity of the LDH monoliths obtained, we added to the LDH powder, when mentioned in the text, some pore-forming silica (amorphous SiO_2) beads and run SPS on the obtained mixture (weight ratio 0.8:0.1 for LDH:SiO_2). The silica beads were preliminarily prepared by sol-gel using the common Stöber methodology. After cold sintering by SPS (see conditions below), the monoliths were soaked at room temperature in NaOH solution 2M for promoting the dissolution of the SiO_2 beads to leave additional open porosity.

2.3. LDH cold sintering: from powders to monoliths

In this work, cold sintering was performed via spark plasma sintering (SPS). The experiments were carried out at the PNF^2 CNRS national platform in link with the CIRIMAT laboratory in Toulouse, France. Experiments were run on either an SPS 2080 or a Dr. Sinter 1050 equipment, both being supplied by Sumitomo Coal Mining Co., Japan. The two machines are indeed interchangeable in the low temperature conditions used in this work. They provide uniaxial pressing and simultaneous heating via DC pulsed current (max. 10 V and 8000 A). In our study, current was limited to 1000 A and a 12 : 2 pulse sequence was used (12 pulses of 3.3 ms followed by two time intervals of 3.3 ms without current). Experiments were run under vacuum, allowing us to detect potential outgassing phenomena. A first run was recorded on sample LDH-L from 25°C to 650°C under 25 MPa mechanical pressure to follow "natural sintering" behavior. Based on the observed outgassing temperature, SPS conditions (sintering temperature, dwell time, applied mechanical pressure) were then modified, as indicated in the text, for a search for optimization, and different sets of conditions were evaluated especially (250°C, 3 min, 25 MPa), (130°C, 3 min, 25 MPa), (130°C, 3 min, 100 MPa) and (130°C, 15 min, 100 MPa). In all cases, a temperature lower or equal to 130 °C was used, thus confirming the "cold sintering approach".

In each experiment, powder LDH (e.g. 0.4 g) was placed in graphite die (e.g. 8 mm internal diameter). A thin graphite foil (Papyex®) was incorporated between the graphite die and the LDH powder for facilitated unmolding after consolidation. The LDH-filled graphite die was transferred into the SPS chamber which was purged under vacuum. During SPS, a heating rate of +100°C/min was used. Mechanical pressure was applied in 1 min.

2.4. Physico-chemical characterization

XRD – The crystal structure of three LDH powders and corresponding sintered monoliths was investigated using X-ray diffractometer (XRD, Bruker AXS D2 Phaser). The scanning range was from 2θ = 5° to 70° with scanning steps of 0.02° under Cu Kα radiation (λ_{Cu} = 1.5406°). Mean crystallite dimensions for each sample were estimated from Scherrer's equation utilizing specific diffraction peaks indicated in the text.

$$\text{Scherrer's equation,} \quad \tau = \frac{0.9\lambda}{B\cos\theta}$$

$$(\lambda = \text{X} - \text{ray wavelength}, \text{B} = \text{full width at half maximum}, \theta = \text{bragg angle})$$

FTIR – Fourier transform infrared (FTIR) spectra were recorded on a Nicolet iS50 spectrometer, in transmission mode, in the 400–4000 cm^{-1} range (64 scans, resolution 4 cm^{-1}) using the KBr pellet method. The spectra were analyzed using the OMNIC software (Thermo Fisher Scientific).

SEM – Particle size and morphology of LDH powders and monoliths were investigated by field emission-scanning electron microscopy (FE-SEM, Quanta 250 FEG, FEI, Hillsboro, OR, USA). Specimens for powder observation were prepared by suspending the LDH in deionized water (0.1 mg/mL) which was drop-casted on pre-cleaned silicon wafer. Sintered LDH monoliths were directly attached on carbon tape for SEM observation without further

treatment. The SEM images were obtained using 30 kV acceleration voltage after surface coating with Pt/Pd sputtering for 60 s.

Zeta potential – The surface charge of LDH powder suspension (1 mg/mL in deionized water) was evaluated with ELSZ-1000 (Otsuka, Kyoto, Japan).

BET surface area and nitrogen (N_2) adsorption – In order to measure the specific surface area and pore size, we carried out N_2 adsorption-desorption isotherm using Belsorp II mini (MICROTRAC BEL CROP., Osaka, Japan) after degassing at 120°C for 12h. Specific surface area and pore size were calculated by BELMASTER based on Brunauer-Emmett-Teller (BET) and Barret-Joyner-Halenda (BJH) method, respectively.

Water adsorption – Water vapor sorption measurements were performed using a home-made device based on manometric measurements (using two capacitive pressure gauges (10 Torr and 1000 Torr). Water vapor sorption was performed at 313 K, each sorption experiment being performed with fresh samples in order to ensure the same initial state of activation of the samples. A duration of 360 s at the same pressure in the sample cell was chosen as criterion for the thermodynamic equilibrium. Longer times of equilibration gave very similar sorption isotherms. Depending on the relative pressure and the sorption process, different equilibration times of adsorption were observed. Furthermore, the determination of the specific surface area as a function of the relative humidity has been performed following procedure presented in Salles *et al.* [27] from experimental adsorption isotherms.

TG/DTA – Thermogravimetry and thermo-differential analyses were run on a Setaram Setsys Evolution thermobalance. Tests were performed in air, from 30 to 900°C, with a heating rate of +5°C/min. The blank experiment consisted in running the same thermal protocol without sample, to correct for Archimedes effect on the air flow.

2.5. Mechanical testing

Taking into account the disc shape of the samples obtained here by SPS cold sintering, compression test standards, which require samples with high height-to-diameter ratios cannot apply here. Therefore, as was frequently done before in the literature on disc-shaped samples, the mechanical behavior of obtained cold-sintered LDH monoliths was inspected in this work on the basis of diametral compression tests, also known as Brazilian disc tests [28]. Mean fracture stress values σ (i.e. maximal load to rupture) were measured by pressing on a diameter of each tested monolith (8 mm diameter, 3.5 mm height), using a Hounsfield press (model H25K-S) equipped with a 25 kN force sensor. In such tests, an increasing force (F) is applied on the disks perpendicular to the cylinder axis until rupture. A loading speed of 0.5 mm/min was used throughout the test for comparative purposes. This leads to tensile strain perpendicular to F, and the corresponding fracture stress value σ, a characteristic of the mechanical strength of the disk, is related to F by the equation:

$$\sigma = \frac{2F}{\pi DH}$$

where D and H are respectively the diameter and height of the disk.

2.6. Computation chemistry

In order to probe the mechanical properties, DFT calculations have been performed with the CASTEP code [29]. The simulations were carried out using the pseudo-potential based plane-wave density functional theory (DFT). The core electrons were replaced by OTFG-ultrasoft pseudopotentials. The functional GGA/PBE was considered. The structures at equilibrium were obtained by using Broyden-Fletcher-Goldfarb-Shenno (BFGS) methods. The convergence criteria were fixed to a value of 1.0×10^{-5} eV/atom; maximum force of 0.03 eV/Å; maximum stress of 0.05 GPa; maximum displacement of 0.001 Å and self consistent field of 1.0×10^{-6} Å.

The bulk modulus values were estimated for MgAl-CO_3-LDH and CaFe-Cl-LDH structures by geometry optimization calculations in the range 0-0.5GPa, starting from the experimental ones obtained from literature [30] and after a preliminary geometry-optimization by imposing no pressure, following the same criteria as previously.

3. Results and discussion

3.1. LDH synthesis with various particle sizes

LDH compounds can be prepared with various combination of metals (**Figure S2**), allowing for a modulation of their properties. A major family of LDHs corresponds to hydrotalcite $Mg_6Al_2(OH)_{16}(CO_3)\cdot 4H_2O$. In this work, such LDHs, denoted MgAl-CO_3-LDH, were synthesized with three particle size scales, so-called small (LDH-S) and medium (LDH-M) prepared by coprecipitation and subsequent hydrothermal treatment, and large (LDH-L) prepared through urea hydrolysis (see experimental details as **Supporting Information**). A typical XRD pattern of prepared LDH powder is given in **Figure 1**. All samples showed crystal structure of hydrotalcite phase (JCPDS No. 14-0191) with well-developed (*00l*) planes (**Figure S3**). Unit cell parameters were similar regardless of primary particle size (**Table S1**). The calculated interlayer spacing before and after cold sintering remained essentially unchanged, at ~0.76 nm (**Figure S3**).

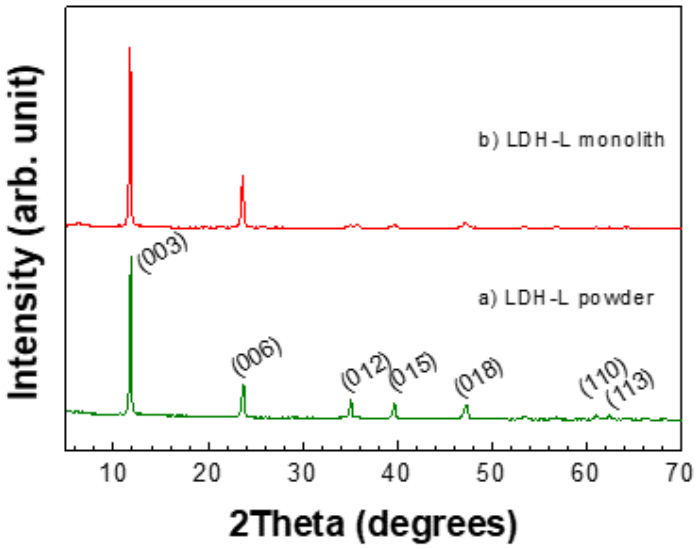

Figure 1. XRD pattern for LDH-L starting precipitated powder (a) and after SPS cold sintering (b). Indexation refers to the hydrotalcite phase (JCPDS No. 14-0191).

3.2.Morphological analyses

The morphology and particle size of precipitated LDHs were assessed by scanning electron microscopy, SEM (**Figure 2**). All three LDH samples had internally-homogeneous size distributions in terms of primary particles in powder state. The average lateral size and thickness of the particles were statistically analyzed from the micrographs from 100 randomly selected particles, indicating lateral size/thickness of (50.4 ± 4.7) nm / (13.5 ± 1.9) nm, (162 ±16.8) nm / (61.0 ± 8.4) nm and (2,650 ± 529) nm / (181 ± 42.6) nm for LDH-S, LDH-M and LDH-L powders, respectively. These findings confirmed the obtainment of three families of particle sizes, roughly around 50, 160 and 2,600 nm. We did not observe significant agglomeration of LDH particles in powder state, with clear coin-like or plate-like single particles (**Figure 2(a)-(c)**). All three LDHs exhibited an anisotropic particle shape with respective aspect ratios of 3.7, 2.6 and 14.6 for LDH-S, LDH-M and LDH-L. When LDH particles exist in powdery or colloidal state, they tend to form networked structure through edge-to-face interaction [31, 32].

We also found similar edge-to-face interaction tendency, which was especially remarkable for the LDH-L powder (**Figure 2(c)**).

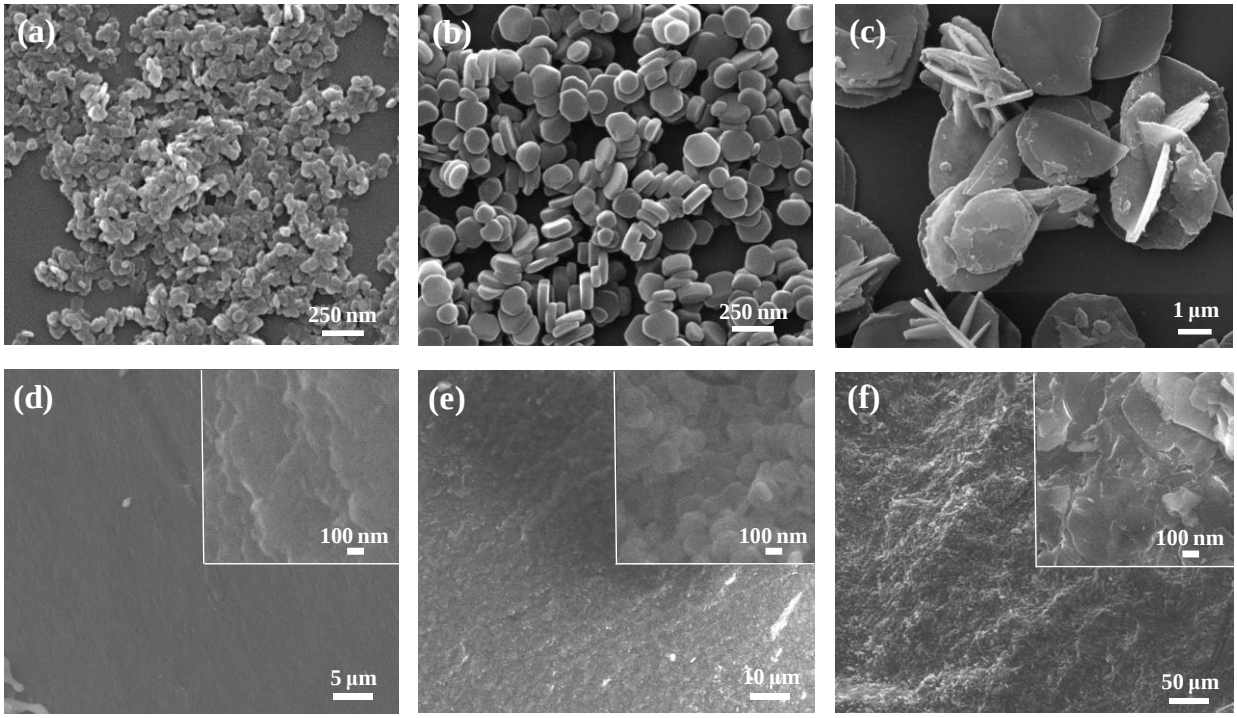

Figure 2. SEM micrographs for (a) LDH-S, (b) LDH-M and (c) LDH-L powders and (d) LDH-S, (e) LDH-M and (f) LDH-L monoliths. Inset images of (d), (e) and (f) were magnified images for LDH monoliths.

3.3. LDH cold sintering: from powder to monoliths

In order to evaluate LDHs initial thermal stability to anticipate their behavior upon consolidation, thermogravimetry (TG) was run (e.g. **Figure S4** for LDH-M). No major weight loss was observed below ca. 130 °C. Three major thermal events were detected at higher temperatures: up to 260 °C (-14.4 wt.%), at 260-360 °C (-9.2 wt.%) and at 360-900 °C (-19.3 wt.%). The first weight loss relates to dehydration with the release of external and interlayer water molecules, which is not directly related to structural change. In contrast, the next two steps are assignable to dehydroxylation and decarbonation generating altering the hydrotalcite structure and ultimately leading to metal oxides [33]. These data served as background to understand thermal behavior of LDH upon SPS.

SPS applied to LDH-L, theoretically the most difficult to consolidate due to high aspect ratio, was undergone with minimal mechanical pressure of 25 MPa and up to 650 °C (under vacuum) to observe the general behavior of the sample. Three outgassing events at 130-280 °C, 280-435 °C and 435-650 °C were detected (**Figure S5**), which can be related to the thermal events detected by TG: no noticeable outgassing occurred below 130 °C. Beyond *ca*. 280 °C, structure decomposition occurred [33]. Several SPS conditions in terms of applied maximal temperature (130 or 250 °C), mechanical pressure (25 or 100 MPa) and dwell time (3 or 15 min) were tested and gas pressure changes and derivatives of displacement of the SPS piston were recorded (**Figure S6**). The following set of SPS conditions was retained: 15 min at 130 °C under 100 MPa for actual monolithic cohesion and no outgassing event. After powder compaction until ~40 °C (**Figure S6(d)**), the second peak in piston displacement relates to the sintering process itself with the formation of strong interparticle bonds. LDHs with different particle sizes (LDH-S and LDH-M samples, **Figures S6(e)** and **(f)** respectively) led to similar outcomes. To our knowledge, this successful preparation of LDH consolidated monoliths has never been reported in literature. **Figure 3** shows, for illustration, an example of obtained cold-sintered LDH monolith.

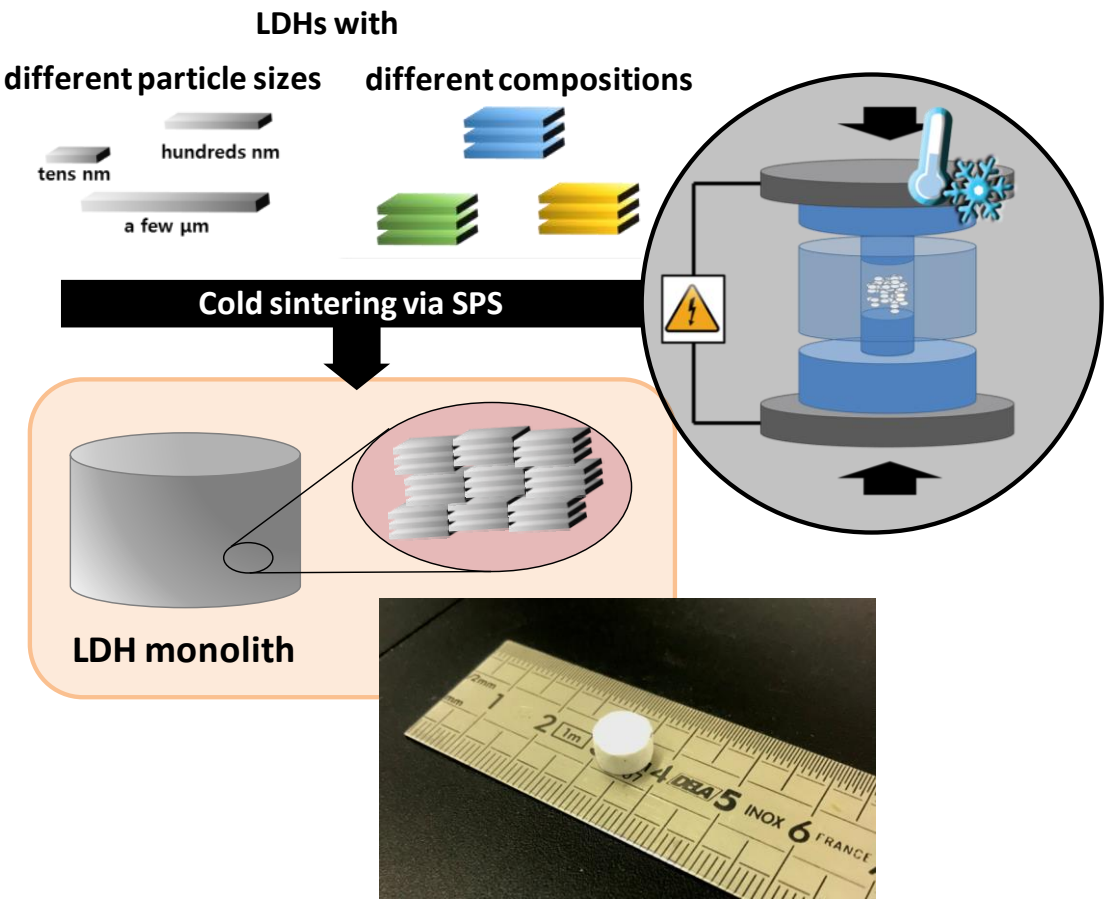

Figure 3. Concept of the study and example of cold-sintered LDH monolith fabricated in this work.

Although XRD confirmed an intact hydrotalcite structure in the monoliths (**Figures 1 and S3**), peaks' full-width at half-maximum remained strongly implied a change in crystallite size. Scherrer's equation led to mean crystallite dimensions summarized in **Table S2**. LDH-L did not show alteration in crystallite size while LDH-S exhibited ~20% increase in *c*-axis and *ab*-plane. LDH-M showed preservation along *ab*-plane but slight reduction in *c*-axis. It implies that small-sized particles (LDH-S) were efficiently consolidated resulting in partial particles growth. Their high surface-to-volume ratio compared with larger ones might be attributed to partial inter-particle fusion. Reduction in crystallite size along c-axis in LDH-M could be explained by partial delamination of layers during SPS. Those small changes in crystallite size did not suggest that LDH was detrimentally destroyed during consolidation. Rather, the results

indicated that the consolidation behaviors of LDH particles are fairly dependent on particle size. As peak intensity is strongly related to the ordering of certain crystal planes, relative intensity before and after consolidation can be originated from the orientation of LDH particles. For all three samples, relative peak intensity showed dramatic increase in (006) and decrease in (110) and (113). Thus, upon SPS (uniaxial pressing) LDH particles aligned in a rather parallel setting along the *c*-axis, leading to textured LDH monoliths (center image of **Figure 3**). This may allow facilitated lateral access to interlayer spaces containing the intercalated anions and water molecules, which can take part in exchange/release processes after immersion.

SEM observation of cold-sintered LDH monoliths clearly evidences efficient densification (**Figure 2(d,e,f)** and **Figure 4**). These micrographs show the densified microstructure obtained after SPS treatment, passing from a powder composed of loosely connected particles to a densified matrix as shown by the highly connected character of the neighboring particles. This is also corroborated by the observation of a pure densification phenomenon after the mechanical compaction of the powder (follow-up of the SPS piston displacement and applied mechanical force, **Figure 4**). By SEM, two obvious morphological changes are seen, in terms of grain boundary and particle arrangement. After cold sintering, grain boundaries became unclear and particles seemed assembled (insets in **Figure 2(d,e,f)**). Plus, these particle assemblies are found throughout the long range surface, suggesting homogeneity in consolidation effect. The consolidation process was most clearly observed for LDH-S, which will be further demonstrated in the specific surface area (SSA) and pore volume section. Also, the arrangement of such anisotropic LDH particles upon sintering was modified. The edge-to-face interaction of the initial powders disappeared in sintered monoliths, LDH particles having aligned in *ab*-plane, in good agreement with XRD data (increase of (006) and decrease of (110) and (113) peak intensities).

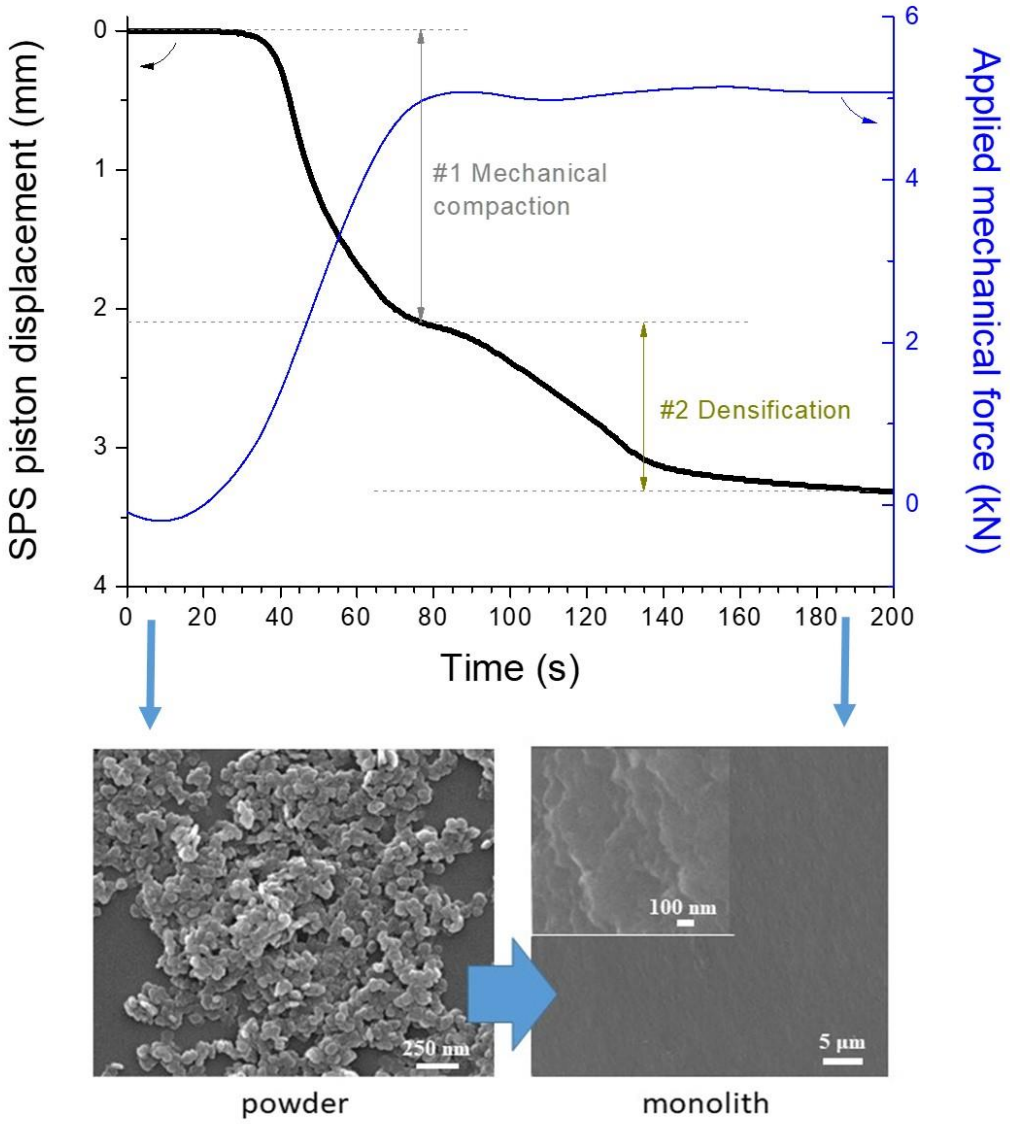

Figure 4. Evidence of consolidation upon SPS for sample LDH-S: follow-up of the piston displacement and applied mechanical force. Event #1 relates to the powder compaction upon applying the mechanical force (100 MPa), event #2 corresponds to the pure LDH consolidation phenomenon. SEM micrographs are also shown before and after sintering.

The IR signature of hydrotalcite remained unchanged after SPS (**Figure S7**), indicating that chemical environments within the LDH structure (i.e. interlayer orientation of carbonate and water or metal-oxygen network) were not significantly modified upon consolidation.

3.4. LDH monoliths: nitrogen and water sorption

N_2 adsorption-desorption isotherms (**Figure S8**) were recorded on powders and monoliths, showing similar type II / III patterns pointing to macroporosity [34, 35]. Low N_2 adsorption at low relative pressure and adsorption abrupt increase at high relative pressure indicated that N_2 adsorption was impossible in interlayer spaces and occurred mainly in macropores from inter-particle spaces [36, 37]. The SSA calculated by BET were 83.4, 29.0 and 61.2 m^2/g for LDH-S, LDH-M and LDH-L, respectively (**Table S3**). The higher SSA of LDH-L than LDH-M may be attributed to house-of-cards structure obtained by plates with large aspect ratios (aspect ratio of LDH-M and LDH-L was 2.6 and 14.6, respectively). Compared with LDH powders, the monoliths of both LDH-S and LDH-M showed dramatic changes in N_2 adsorption amount and adsorption-desorption hysteresis. The N_2 adsorbed amount on monoliths (**Figures S8(d,e)**) dramatically reduced compared with starting powders (**Figures S8(a,b)**) depicting reduction in exposed particle surface and pore volume, leading to successful consolidation between particles. The reduction in particles exposed surface was strongly reflected by the decrease in SSA (83.4 m^2/g to 1.49 m^2/g for LDH-S and 29.0 m^2/g to 14.9 m^2/g for LDH-M). Hysteresis – not noticed for powders – was clearly observed in the LDH-S and LDH-M monoliths, indicating different pore shapes inside the monoliths and at their periphery. It also indicated the effective formation of particle-to-particle network upon consolidation. The N_2 adsorption-desorption pattern of LDH-L before and after SPS was slightly different. Although the hysteresis increased slightly after SPS (**Figures S8(c,f)**), there were no significant changes in adsorbed volume nor SSA (**Table S3**).

Contrary to N_2, the water probe can also visit the interlayer spaces due to strong interaction between water molecules and interlayer anions. The impact of the sinterability can thus be evaluated by measuring the adsorption water isotherms for the shaped solids.

Water sorption isotherms (**Figure 5**) exhibit similar features, as they originate from the same LDH composition. For instance, the shape at low relative pressure can be related to the affinity of the LDH surface towards water. The hysteresis loops are also present for the three materials, but stronger for LDH-S. Additionally, the desorption branches do not reach the adsorption branches, back to low relative pressure, which shows that water is in strong interaction with the LDH materials, leading to some sorption irreversibility. However, some differences deserve to be discussed. If H_2O sorption at low relative pressure is similar for the three LDH materials, at high relative pressure, however, LDH-S isotherm exhibits a different shape. From $p/p°=0.6$, there is no saturation, contrarily to LDH-M and LDH-L. This shows that water can be adsorbed to a greater extent in LDH-S, likely by capillary condensation. In fact, sintering a material made of small particles likely generates small voids which can be filled with water. Thus, it can be concluded that for LDH-M and LDH-L, capillary condensation does not occur in the pressure range investigated. This pore size dependency towards capillary condensation has been documented in the past [38, 39]. However, because of technical limitations, we could not explore very high relative pressure for avoiding water liquefaction in the sorption device. Compared to their textural properties, as probed by nitrogen at 77K, the sintered LDH materials are able to adsorb large amounts of water, typically, 15 wt % at saturation. This emphasizes their ability to allow water adsorption in their structures even after shaping. This behavior is confirmed by the determination of the SSA as a function of the relative humidity [27]. Indeed the evolution of the SSA evidences the impact of the size of the particles, since the SSA for LDH-S is lower than for LDH-M and LDH-L. This difference can be explained by the stronger sintering of LDH-S. Therefore, even if the sintered materials do undergo a dramatic loss of SSA, they are still able to interact with water in a quantitative way.

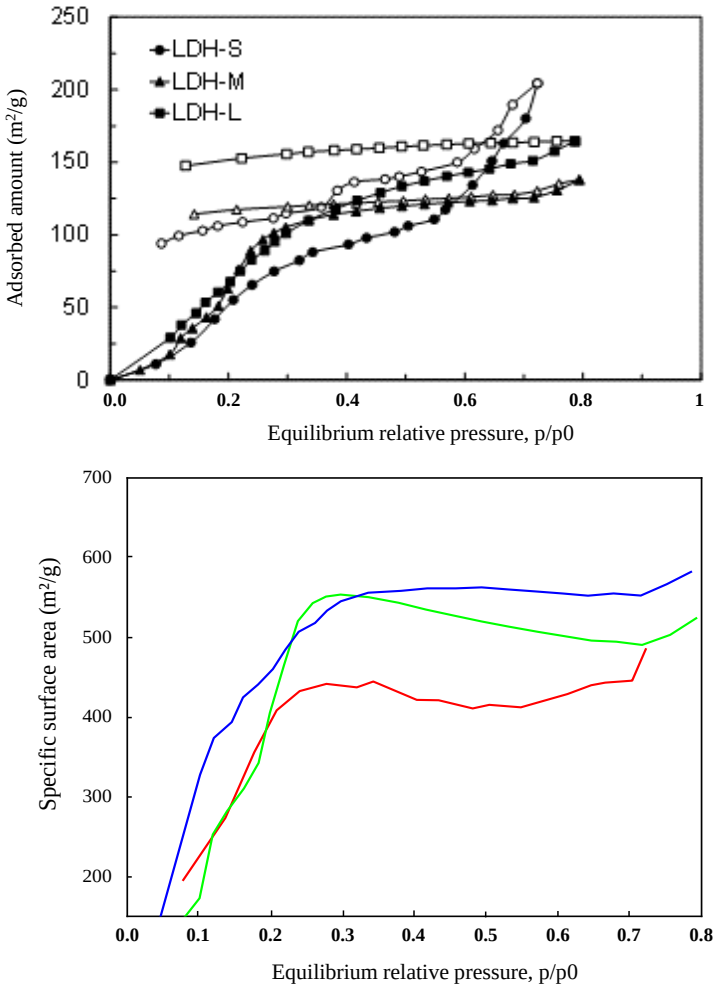

Figure 5. Water vapor adsorption isotherms for the different sized samples and corresponding evolution of the specific surface area following the procedure described in Salles *et al.* [2]

3.5. Mechanical behavior

The monoliths (pellet shape) were evaluated from a mechanical point of view using diametral compression tests [28], as done before for example of cold-sintered nanocrystalline apatites [23] or amorphous calcium phosphates [40]. The mean fracture stress values σ (i.e. maximal load to rupture) were measured at (5.7 ± 1.3 MPa), (2.5 ± 1.0 MPa) and (6.9 ± 1.5 MPa) respectively for LDH-S, -M and -L. These values have, however, to be related to the apparent density of the monoliths, which were measured as 1.98, 1.33 and 1.76 g/cm^3. Considering that hydrotalcite has a theoretical absolute density of 2 g/cm^3 [41], this leads to densification rates via SPS cold sintering of 99 %, 67 % and 88 %, respectively for LDH-S, -M and -L. These

results confirm the conclusions drawn by XRD and SEM, showing that the LDH-S sample was the most efficiently consolidated. In all cases, the monoliths obtained can easily be manipulated and cut into large chunks (no loose powder) after mechanical testing.

Thus, cold sintering by SPS at 130 °C / 15 min / 100 MPa are cooperative conditions to allow actual monolith formation from hydrotalcite-type LDHs with different characteristics.

3.6. Extension to other LDH structures and compositions

For enlarging the proof of concept to other LDH compositions, we considered also two other types of compounds: MgFe-CO_3-LDH (pyroaurite crystal structure, $Mg_6Fe_2(OH)_{16}CO_3{\cdot}4.5H_2O$) and CaFe-Cl-LDH (hydrocalumite-like crystal structure, $Ca_2Fe(OH)_6Cl{\cdot}2H_2O$). These compounds were synthesized by coprecipitation (see experimental section in SI) and cold-sintered using the same optimized parameters as above. Again, consolidated monoliths were successfully obtained, reaching for example 83 % of densification for the CaFe-Cl-LDH monolith (using the accessible calculated density from this compound, from ICSD ID file 82280). XRD showed that the initial crystallographic structures and related unit cell parameters were preserved after sintering (**Figures S9** and **S10**) and SEM observations pointed out again an efficient consolidation (**Figures S11** and **S12**). Diametral compression tests led to mean fracture stress values σ of 11.5 ± 3.4 MPa and 8.3 ± 1.5 MPa, respectively, for MgFe-CO_3-LDH and CaFe-Cl-LDH. These values are even greater than those obtained for hydrotalcite, demonstrating that i) consolidation by SPS cold sintering at 130 °C is effective on several LDH structures and compositions and ii) the mechanical resistance of obtained monoliths varies with the type of LDH. Note that these σ values are of the same order as those obtained for cold-sintered calcium phosphates [22, 23, 40]. The possibility to further modulate the porosity of obtained monoliths was checked by adding a pore-forming agent before SPS, namely amorphous SiO_2 silica beads prepared by Stöber sol-gel. After cold

sintering, the monoliths were immersed in NaOH aqueous solution to dissolve specifically the SiO_2 particles (leaving open pores) while preserving the LDH networks. SEM confirmed the presence of pores even in the section of the monoliths (**Figures S13**). This strategy may allow modulating the overall porosity of LDH monoliths to finely tune the accessibility for surrounding fluids.

3.7. Discussion on LDH cold sintering mechanism

Sintering consists in joining particles together without melting. Reduction of the total interfacial energy is the thermodynamic driving force, made possible via mass transfer. This is favored by diffusion phenomena and grain plasticity when relevant. Sintering initiates at regions where particles are in contact with each other, progressively forming interconnected pore channels (densification rates of 65-90 % are generally admitted for this intermediate sintering stage). As sintering proceeds toward 100 %, these channels get progressively disconnected, leading to isolated pores until disappearing. In the meantime, mass transfer allows grain growth. In cold sintering, diffusion is, however, not thermally activated, and a "mass transfer phase" is usually needed to facilitate mass transfer [24]. It is generally a phase that is liquid at some point in the sintering process. In LDHs, an important amount of water is present, essentially in interlayer spaces. One possible mechanistic scheme could involve the local release of some of the interlayer water which could momentarily act as transport phase taking part in the sintering process by favoring ion diffusion. However, our experiments showed that LDH sintering was not associated with any outgassing at the limited temperature considered here, thus no quantitative water release occurred. If H_2O is implicated in the sintering process of LDHs, the effect likely remains at a local scale near grain boundaries to favor matter diffusion. Local water release could also favor dissolution-reprecipitation allowing densification. A second mechanistic scheme could involve the mobilization of some ions (possibly combined to H_2O

molecules), probably from the external edges of LDH particles, which could momentarily form a liquid phase. Indeed the determination of the bulk modulus from DFT calculations (see SI) has proved that the theoretical values obtained for dry CaFe-Cl (93 GPa) and dry Mg-Al-CO_3 (169 GPa) are strongly impacted by both the composition of the layers and the nature of the interlayer anions. Experimentally, it has been proved that the compensating anions have an impact on the structure of the interlayer space since divalent anions (such as CO_3^{2-}) strongly interact with the layers and limit the swelling. It follows therefore that the presence of carbonates should rigidify the interlayer spaces and favor the sinterability. In addition it has been observed that some forms of hydrated calcium chloride are known to melt at very low temperatures, around 30 °C for $CaCl_2 \cdot 6H_2O$ and 45 °C for $CaCl_2 \cdot 4H_2O$ [42]. Under cold sintering at 130 °C, such compounds could form locally in liquid state and participate to the effective formation of grain boundaries and interparticle bonds. SEM observation of monolith sections did not show any peculiarities (**Figure S13**). But based on the above mechanistic reflection, we analyzed more specifically the monolith external surfaces. Interestingly, the presence of micron-sized particles could then be detected (**Figure S14**). These particles were not observed for the other two LDH compositions, and are thus related to the presence of chloride. Their observation on the external surface of the CaFe-Cl-LDH monoliths – and not in the monolith section – might be linked to the higher temperatures reached locally on contact with the SPS mold. These microparticles most likely correspond to the above-mentioned calcium chloride hydrates that exhibit exceptionally low melting temperatures. The eventuality for such phases to form also locally inside the monolith during sintering (and favor inter-particle bonding) cannot be ruled out even if these particles are no more detectable after cooling. In this hypothesis, the nature of the transport liquid phase would depend greatly on their ionic contents. This could explain in part our observed differences in densification rate and mechanical resistance for different LDH compositions; however, all LDHs tested yielded densified

monoliths. Further systematic studies on LDH cold sintering will allow shedding more light on such mechanistic aspects. It is worth noting, in any case, that XRD and FTIR showed no significant modification in overall structure and composition for the three different types of LDHs tested here (hydrotalcite, pyroaurite and hydrocalumite). Therefore, possible modifications in the particles chemistry, if any, are likely to remain localized after cooling.

4. Conclusions

LDHs are layered inorganic compounds relevant to a large range of applicative fields, thanks to their ability to incorporate/deliver ions and molecular species in their interlayer spaces. However, LDHs have so far been used essentially as separate particles and suspensions in link with their metastability precluding the use of conventional sintering strategies to prepare cohesive monoliths, and therefore preventing applications needing 3D scaffolds. In this work, we demonstrate for the first time that cold sintering by SPS at typically 130 °C allows for the successful fabrication of cohesive LDH monoliths. We also demonstrate that such consolidation may be extended to several starting LDHs with various structures, particle sizes and ionic compositions. Chemical and structural features of initial powders are shown to be preserved, while densification rates often larger than 80 % are reached pointing out cohesive particle arrangements. The monoliths were tested mechanically to assess their cohesiveness. For a given LDH type, minimization of particle size is found to allow greater cohesion and texturation along the c-axis indicating more efficient alignment of adjacent layered particles.

LDH compounds encompass an important amount of water in interlayer spaces prone to take part in the mass transport phase during cold sintering by favoring ion diffusion. However, our data show that LDH cold sintering is not associated with quantitative water release. Thus, H_2O molecules may operate more locally, at grain boundaries, to facilitate diffusion and/or dissolution-reprecipitation favoring densification. The chemical composition of the starting

LDH powder is shown to have a direct impact on the consolidation mechanism and on the nature of the possible transport liquid phase involved during LDH cold sintering. For Cl-containing LDHs, in particular, the local formation of calcium chloride hydrates after SPS is conjecture based on our observations.

The cohesive LDH monoliths obtained are able to interact with small molecules such as water "in a quantitative way", thus evidencing the relevance of this consolidation process which is capable of retaining LDH reactivity. Also, we show that it is possible to modulate the microstructure/porous network by adding pore-forming agents to tune the interfacial contact surface with the surrounding medium, e.g. in view of the targeted applicative purposes.

By identifying an effective strategy for LDH consolidation, thus overcoming a current technological challenge, this work allows envisioning new applications of LDHs where 3D solid materials are particularly pertinent, as in electrodes and sensors technology, energy storage, heterogeneous catalysis, orthopedic biomaterials or else waste remediation membranes, among other fields.

Acknowledgements

The authors thank the Hubert Curien (PHC) partnership program for funding of the STAR project via Campus France. This research was supported under the framework of International Cooperation Program managed by the National Research Foundation of Korea [NRF-2017K1A3A1A21013758].

Author Contributions

HJK, THK, JS and SC: Investigation; Formal Analysis; Data curation; Writing – review & editing. FS: Methodology; Formal Analysis; Data curation; Writing – original draft. GC, CT and PT: Formal Analysis; Data curation. JMO and CD: Investigation; Methodology; Formal

Analysis; Data curation; Writing – original draft; Conceptualization; Funding acquisition; Project administration.

Conflicts of interest

There are no conflicts to declare.

Data availability

The raw/processed data required to reproduce these findings cannot be shared at this time as the data also forms part of an ongoing study.

References

[1] F. Dionigi *et al.*, "In-situ structure and catalytic mechanism of NiFe and CoFe layered double hydroxides during oxygen evolution," *Nature Communications*, vol. 11, no. 1, p. 2522, 2020/05/20 2020, doi: 10.1038/s41467-020-16237-1.

[2] C. Forano, U. Costantino, V. Prévot, and C. T. Gueho, "Chapter 14.1 - Layered Double Hydroxides (LDH)," in *Developments in Clay Science*, vol. 5, F. Bergaya and G. Lagaly Eds.: Elsevier, 2013, pp. 745-782.

[3] S. Tang, Y. Yao, T. Chen, D. Kong, W. Shen, and H. K. Lee, "Recent advances in the application of layered double hydroxides in analytical chemistry: A review," *Analytica Chimica Acta*, vol. 1103, pp. 32-48, 2020/03/22/ 2020, doi: https://doi.org/10.1016/j.aca.2019.12.065.

[4] J. Yu, Q. Wang, D. O'Hare, and L. Sun, "Preparation of two dimensional layered double hydroxide nanosheets and their applications," *Chemical Society Reviews*, 10.1039/C7CS00318H vol. 46, no. 19, pp. 5950-5974, 2017, doi: 10.1039/C7CS00318H.

[5] G. H. Gwak, M. K. Kim, and J. M. Oh, "Composites of Quasi-Colloidal Layered Double Hydroxide Nanoparticles and Agarose Hydrogels for Chromate Removal," (in eng), *Nanomaterials (Basel)*, vol. 6, no. 2, Jan 26 2016, doi: 10.3390/nano6020025.

[6] S. Song *et al.*, "New Way to Synthesize Robust and Porous Ni1–xFex Layered Double Hydroxide for Efficient Electrocatalytic Oxygen Evolution," *ACS Applied Materials & Interfaces*, vol. 11, no. 36, pp. 32909-32916, 2019/09/11 2019, doi: 10.1021/acsami.9b08194.

[7] Y. Guo *et al.*, "Multicomponent Hierarchical Cu-Doped NiCo-LDH/CuO Double Arrays for Ultralong-Life Hybrid Fiber Supercapacitor," *Advanced Functional*

Materials, https://doi.org/10.1002/adfm.201809004 vol. 29, no. 24, p. 1809004, 2019/06/01 2019, doi: https://doi.org/10.1002/adfm.201809004.

[8] Y. Tokudome *et al.*, "Layered Double Hydroxide Nanoclusters: Aqueous, Concentrated, Stable, and Catalytically Active Colloids toward Green Chemistry," *ACS Nano*, vol. 10, no. 5, pp. 5550-5559, 2016/05/24 2016, doi: 10.1021/acsnano.6b02110.

[9] X. Han *et al.*, "Mass and Charge Transfer Coenhanced Oxygen Evolution Behaviors in CoFe-Layered Double Hydroxide Assembled on Graphene," *Advanced Materials Interfaces*, https://doi.org/10.1002/admi.201500782 vol. 3, no. 7, p. 1500782, 2016/04/01 2016, doi: https://doi.org/10.1002/admi.201500782.

[10] S. Ma *et al.*, "Highly selective and efficient heavy metal capture with polysulfide intercalated layered double hydroxides," *Journal of Materials Chemistry A*, 10.1039/C4TA01203H vol. 2, no. 26, pp. 10280-10289, 2014, doi: 10.1039/C4TA01203H.

[11] F. Barahuie, Z. M. Hussein, S. Fakurazi, and Z. Zainal, "Development of Drug Delivery Systems Based on Layered Hydroxides for Nanomedicine," *International Journal of Molecular Sciences*, vol. 15, no. 5, 2014, doi: 10.3390/ijms15057750.

[12] X. Bi, H. Zhang, and L. Dou, "Layered Double Hydroxide-Based Nanocarriers for Drug Delivery," *Pharmaceutics*, vol. 6, no. 2, 2014, doi: 10.3390/pharmaceutics6020298.

[13] J. H. Choy *et al.*, "Layered double hydroxide as an efficient drug reservoir for folate derivatives," (in eng), *Biomaterials*, vol. 25, no. 15, pp. 3059-64, Jul 2004, doi: 10.1016/j.biomaterials.2003.09.083.

[14] H.-J. Kim, J. Y. Lee, T.-H. Kim, G.-H. Gwak, J. H. Park, and J.-M. Oh, "Radioisotope and anticancer agent incorporated layered double hydroxide for tumor targeting

theranostic nanomedicine," *Applied Clay Science*, vol. 186, p. 105454, 2020/03/01/ 2020, doi: https://doi.org/10.1016/j.clay.2020.105454.

[15] S. Han *et al.*, "Hierarchically porous cobalt aluminum layered double hydroxide flowers with enhanced capacitance performances," *Journal of Materials Science*, vol. 52, no. 10, pp. 6081-6092, 2017/05/01 2017, doi: 10.1007/s10853-017-0847-6.

[16] J. Prince, A. Montoya, G. Ferrat, and J. S. Valente, "Proposed General Sol−Gel Method to Prepare Multimetallic Layered Double Hydroxides: Synthesis, Characterization, and Envisaged Application," *Chemistry of Materials*, vol. 21, no. 24, pp. 5826-5835, 2009/12/22 2009, doi: 10.1021/cm902741c.

[17] J. Zheng *et al.*, "Integrated MXene-based Aerogel Composite: Componential and Structural Engineering towards Enhanced Performance Stability of Hybrid Supercapacitor," *Chemical Engineering Journal*, p. 125197, 2020/04/29/ 2020, doi: https://doi.org/10.1016/j.cej.2020.125197.

[18] N. Sonoyama, K. Takagi, S. Yoshida, T. Ota, P. D. Kimilita, and Y. Ogasawara, "Optical properties of the europium (II) and (III) ions doped metal oxides obtained from sintering layered double hydroxides, and their fine structures," *Applied Clay Science*, vol. 186, p. 105440, 2020/03/01/ 2020, doi: https://doi.org/10.1016/j.clay.2020.105440.

[19] N. Tarutani, Y. Tokudome, M. Fukui, K. Nakanishi, and M. Takahashi, "Fabrication of hierarchically porous monolithic layered double hydroxide composites with tunable microcages for effective oxyanion adsorption," *RSC Advances*, 10.1039/C5RA05942A vol. 5, no. 70, pp. 57187-57192, 2015, doi: 10.1039/C5RA05942A.

[20] Y. Tokudome, N. Tarutani, K. Nakanishi, and M. Takahashi, "Layered double hydroxide (LDH)-based monolith with interconnected hierarchical channels: enhanced sorption affinity for anionic species," *Journal of Materials Chemistry A*,

10.1039/C3TA11110E vol. 1, no. 26, pp. 7702-7708, 2013, doi: 10.1039/C3TA11110E.

[21] D. Grossin *et al.*, "Biomimetic apatite sintered at very low temperature by spark plasma sintering: Physico-chemistry and microstructure aspects," *Acta Biomaterialia*, vol. 6, no. 2, pp. 577-585, 2010 2010, doi: 10.1016/j.actbio.2009.08.021.

[22] C. Drouet *et al.*, "Bioceramics: Spark Plasma Sintering (SPS) of Calcium Phosphates," in *Advances in Science and Technology*, ed: CrossRef Test Account, 2006, pp. 45--50.

[23] C. Drouet *et al.*, "Nanocrystalline apatites: From powders to biomaterials," *Powder Technology*, vol. 190, no. 1-2, pp. 118-122, 2009 2009, doi: 10.1016/j.powtec.2008.04.041.

[24] J. Guo *et al.*, "Cold Sintering: Progress, Challenges, and Future Opportunities," *Annual Review of Materials Research*, vol. 49, no. 1, pp. 275-295, 2019/07/01 2019, doi: 10.1146/annurev-matsci-070218-010041.

[25] S. Grasso *et al.*, "A review of cold sintering processes," *Advances in Applied Ceramics*, vol. 119, no. 3, pp. 115-143, 2020/04/02 2020, doi: 10.1080/17436753.2019.1706825.

[26] S. H. Bang, T. Herisson De Beauvoir, and C. A. Randall, "Densification of thermodynamically unstable tin monoxide using cold sintering process," *Journal of the European Ceramic Society*, vol. 39, no. 4, pp. 1230-1236, 2019/04/01/ 2019, doi: https://doi.org/10.1016/j.jeurceramsoc.2018.11.026.

[27] F. Salles *et al.*, "Hydration sequence of swelling clays: Evolutions of specific surface area and hydration energy," *Journal of Colloid and Interface Science*, vol. 333, no. 2, pp. 510-522, 2009/05/15/ 2009, doi: https://doi.org/10.1016/j.jcis.2009.02.018.

[28] A. Brückner-Foit, T. Fett, D. Munz, and K. Schirmer, "Discrimination of multiaxiality criteria with the Brazilian disc test," *Journal of the European Ceramic Society*, vol.

17, no. 5, pp. 689-696, 1997/01/01/ 1997, doi: https://doi.org/10.1016/S0955-2219(96)00085-4.

[29] M. D. Segall *et al.*, "First-principles simulation: ideas, illustrations and the CASTEP code," *Journal of Physics: Condensed Matter*, vol. 14, no. 11, pp. 2717-2744, 2002/03/08 2002, doi: 10.1088/0953-8984/14/11/301.

[30] I. Rousselot, C. Taviot-Guého, F. Leroux, P. Léone, P. Palvadeau, and J.-P. Besse, "Insights on the Structural Chemistry of Hydrocalumite and Hydrotalcite-like Materials: Investigation of the Series Ca2M3+(OH)6Cl·2H2O (M3+: Al3+, Ga3+, Fe3+, and Sc3+) by X-Ray Powder Diffraction," *Journal of Solid State Chemistry*, vol. 167, no. 1, pp. 137-144, 2002/08/01/ 2002, doi: https://doi.org/10.1006/jssc.2002.9635.

[31] H. van Olphen, "Internal mutual flocculation in clay suspensions," *Journal of Colloid Science*, vol. 19, no. 4, pp. 313-322, 1964/04/01/ 1964, doi: https://doi.org/10.1016/0095-8522(64)90033-9.

[32] Y. Furukawa, J. L. Watkins, J. Kim, K. J. Curry, and R. H. Bennett, "Aggregation of montmorillonite and organic matter in aqueous media containing artificial seawater," *Geochemical Transactions*, vol. 10, no. 1, p. 2, 2009/01/23 2009, doi: 10.1186/1467-4866-10-2.

[33] F. Millange, R. I. Walton, and D. O'Hare, "Time-resolved in situ X-ray diffraction study of the liquid-phase reconstruction of Mg–Al–carbonate hydrotalcite-like compounds," *Journal of Materials Chemistry*, 10.1039/B002827O vol. 10, no. 7, pp. 1713-1720, 2000, doi: 10.1039/B002827O.

[34] N. Ponomarev and M. Sillanpää, "Combined chemical-templated activation of hydrolytic lignin for producing porous carbon," *Industrial Crops and Products*, vol. 135, pp. 30-38, 2019/09/01/ 2019, doi: https://doi.org/10.1016/j.indcrop.2019.03.050.

[35] S. Ismadji, F. E. Soetaredjo, and A. Ayucitra, *Clay Materials for Environmental Remediation* (SpringerBriefs in Molecular Science). Springer International Publishing, 2015.

[36] B.-K. Kim, G.-H. Gwak, T. Okada, and J.-M. Oh, "Effect of particle size and local disorder on specific surface area of layered double hydroxides upon calcination-reconstruction," *Journal of Solid State Chemistry*, vol. 263, pp. 60-64, 2018/07/01/ 2018, doi: https://doi.org/10.1016/j.jssc.2018.03.041.

[37] X. Guo, P. Yin, and H. Yang, "Superb adsorption of organic dyes from aqueous solution on hierarchically porous composites constructed by ZnAl-LDH/Al(OH)3 nanosheets," *Microporous and Mesoporous Materials*, vol. 259, pp. 123-133, 2018/03/15/ 2018, doi: https://doi.org/10.1016/j.micromeso.2017.10.003.

[38] K. Morishige and Y. Nakamura, "Nature of Adsorption and Desorption Branches in Cylindrical Pores," *Langmuir*, vol. 20, no. 11, pp. 4503-4506, 2004/05/01 2004, doi: 10.1021/la030414g.

[39] P. Trens, N. Tanchoux, D. Maldonado, A. Galarneau, F. Di Renzo, and F. Fajula, "Study of n-hexane adsorption in MCM-41 mesoporous materials: a scaling effect approach of capillary condensation processes," *New Journal of Chemistry*, 10.1039/B401094A vol. 28, no. 7, pp. 874-879, 2004, doi: 10.1039/B401094A.

[40] M. Luginina *et al.*, "First successful stabilization of consolidated amorphous calcium phosphate (ACP) by cold sintering: toward highly-resorbable reactive bioceramics," *Journal of Materials Chemistry B*, 10.1039/C9TB02121C vol. 8, no. 4, pp. 629-635, 2020, doi: 10.1039/C9TB02121C.

[41] V. Rives, *Layered Double Hydroxides: Present and Future*. Nova Science Publishers, 2001.

[42] D. E. Garrett, "Part 2 - Calcium Chloride," in *Handbook of Lithium and Natural Calcium Chloride*, D. E. Garrett Ed. Oxford: Academic Press, 2004, pp. 237-457.